


# Self-powered horizontally structured n-n heterojunction photodetector based on Si-GaN/$\beta$-$Ga_2O_3$ for UV detection

Muzi Li(李木子), Maolin Zhang(张茂林), Xueqiang Ji(季学强), Shan Li(李山), Lili Yang(杨莉莉), and Weihua Tang(唐为华)

**Citation:**Chin. Phys. B, 2026, 35 (**2**): 028502. DOI: 10.1088/1674-1056/adee8d
http://cpb.iphy.ac.cn; http://iopscience.iop.org/cpb

**What follows is a list of articles you may be interested in**

---

## $\beta$-$Ga_2O_3$/BP heterojunction for deep ultraviolet and infrared narrowband dual-band photodetection

Zhichao Chen(陈志超), Feng Ji(季枫), Yadan Li(李亚丹), Yahan Wang(王雅涵), Xuehao Ge(葛薛豪), Kai Jiang(姜凯), Hai Zhu(朱海), and Xianghu Wang(王相虎)

Chin. Phys. B, 2025, 34 (**12**): 128501. DOI: 10.1088/1674-1056/adea9d

## Self-powered broadband photodetector based on pyramid-structured Si/$TiO_2$ heterojunction

Leyao Wu(吴乐瑶), Xinnan Shi(师馨楠), Haibo Fan(范海波), Qiujie Li(李秋洁), Peng Hu(胡鹏), and Feng Teng(滕凤)

Chin. Phys. B, 2025, 34 (**8**): 088501. DOI: 10.1088/1674-1056/add50a

## A fast-response self-powered UV-Vis-NIR broadband photodetector based on a $AgIn_5Se_8$/t-Se heterojunction

Kang Li(李康), Lei Xu(许磊), Qidong Lu(陆启东), and Peng Hu(胡鹏)

Chin. Phys. B, 2023, 32 (**11**): 118503. DOI: 10.1088/1674-1056/acec44

## Fast-speed self-powered PEDOT: PSS/$\alpha$-$Ga_2O_3$ nanorod array/FTO photodetector with solar-blind UV/visible dual-band photodetection

Ming-Ming Fan(范明明), Kang-Li Xu(许康丽), Ling Cao(曹铃), and Xiu-Yan Li(李秀燕)

Chin. Phys. B, 2022, 31 (**4**): 048501. DOI: 10.1088/1674-1056/ac3814

## High performance $Cu_2O$ film/ZnO nanowires self-powered photodetector by electrochemical deposition

Deshuang Guo(郭德双), Wei Li(李微), Dengkui Wang(王登魁), Bingheng Meng(孟兵恒), Dan Fang(房丹), Zhipeng Wei(魏志鹏)

Chin. Phys. B, 2020, 29 (**9**): 098504. DOI: 10.1088/1674-1056/aba610

---

# Self-powered horizontally structured n–n heterojunction photodetector based on Si–GaN/$\beta$-$Ga_2O_3$ for UV detection

Muzi Li(李木子), Maolin Zhang(张茂林), Xueqiang Ji(季学强), Shan Li(李山), Lili Yang(杨莉莉)†, and Weihua Tang(唐为华)‡

*Innovation Center for Gallium Oxide Semiconductor (IC-GAO), College of Integrated Circuit Science and Engineering, Nanjing University of Posts and Telecommunications, Nanjing* 210023, *China*

(Received 19 May 2025; revised manuscript received 22 June 2025; accepted manuscript online 11 July 2025)

With the rapid advancement of optoelectronic technology, high-performance photodetectors are increasingly in demand in fields such as environmental monitoring, optical communication, and defense systems, where ultraviolet detection is critical. However, conventional semiconductor materials suffer from limited UV-visible detection capabilities owing to their narrow bandgaps and high dark currents. To address these challenges, wide-bandgap semiconductors have emerged as promising alternatives. Here, we fabricated a horizontally structured n–n heterojunction photodetector by growing $\beta$-$Ga_2O_3$ on Si–GaN via plasma-enhanced chemical vapor deposition. The device exhibits a self-powered photocurrent of 3.5 nA at zero bias, enabled by the photovoltaic effect of the space charge region. Under 254-nm and 365-nm illumination, it exhibits rectification behavior, achieving a responsivity of 0.475 mA/W (0 V, 220 μW/cm$^2$ at 254 nm) and 257.6 mA/W ($-5$ V), respectively. Notably, the photodetector demonstrates a high photocurrent-to-dark current ratio of $10^5$ under $-5$-V bias, highlighting its potential for self-powered and high-performance UV detection applications.

**Keywords:** Si–GaN/$\beta$-$Ga_2O_3$, horizontally structured, n–n heterojunction, self-powered

**PACS:** 85.30.–z, 85.30.De, 85.25.–j

**DOI:** 10.1088/1674-1056/adee8d **CSTR:** 32038.14.CPB.adee8d

## 1. Introduction

In recent years, remarkable progress in optoelectronic technology has driven significant advances in high-performance photodetectors, enabling diverse applications ranging from environmental monitoring to defense systems.[1,2] While conventional semiconductors such as silicon and gallium arsenide have served as fundamental materials, their limited bandgaps and carrier mobilities restrict their performance in ultraviolet-to-visible spectral detection.[3] This challenge has motivated substantial research into wide-bandgap semiconductors, particularly gallium nitride (GaN) and gallium oxide ($Ga_2O_3$), which offer superior physical and chemical properties.[4–7]

GaN has exceptional characteristics including a direct bandgap of 3.4 eV and high electron saturation velocity, whereas $Ga_2O_3$ has an ultra-wide bandgap ($\sim$ 4.9 eV) making it particularly suitable for deep-ultraviolet detection.[8–11] Among its polymorphs, $\beta$-$Ga_2O_3$ stands out for its excellent thermal and chemical stability, making it ideal for operation in extreme environments involving high temperatures and radiation.[2,12]

The performance of lateral heterojunction photodetectors critically depends on the conductivity of materials. While Mg-doped GaN typically suffers from high resistivity which hinders efficient carrier extraction,[9] Si-doped n-type GaN has proven effective in reducing resistivity without compromising optoelectronic performance.[13] This understanding led to our innovative approach of constructing an n–n heterojunction using n-type-doped GaN and intrinsic n-type $Ga_2O_3$. Through precise energy band alignment engineering, we achieved performance comparable to conventional p–n junction photodetectors.

This study employed plasma-enhanced chemical vapor deposition (PECVD) to epitaxially grow $\beta$-$Ga_2O_3$ on Si–GaN substrates and fabricated a horizontally structured n–n heterojunction photodetector. The device demonstrated excellent performance metrics, including a specific detectivity ($D^*$) of $8.6 \times 10^8$ Jones and responsivity ($R$) of 0.475 mA/W under 254-nm illumination (220 μW/cm$^2$) at zero bias. Notably, at a bias of $-5$ V, the device observes an outstanding photo-to-dark current ratio (PDCR) of $10^5$. These results not only validate the potential of n–n heterojunction architectures for high-performance optoelectronics but also open new avenues for device optimization and application development in this field.

## 2. Experimental details

The $\beta$-$Ga_2O_3$ thin film was deposited via plasma-enhanced chemical vapor deposition (PECVD) on a pre-patterned sapphire substrate with a pre-grown Si-doped GaN epitaxial layer.[14,15] High-purity gallium particles

†Corresponding author. E-mail: liliyang@njupt.edu.cn

‡Corresponding author. E-mail: whtang@njupt.edu.cn

© 2026 Chinese Physical Society and IOP Publishing Ltd. All rights, including for text and data mining, AI training, and similar technologies, are reserved.

(99.99999%) and oxygen gas were used as precursors, with argon (Ar) as the carrier gas. The deposition process was conducted at approximately 870 °C for 45 min, with the radio frequency (RF) power, oxygen flow rate, and argon flow rate maintained at 250 W, 20 sccm, and 20 sccm, respectively. As illustrated in Fig. 1(a), a horizontal n–n heterojunction structure was successfully fabricated. Subsequently, two indium electrodes (1 mm×1 mm) were deposited on the film surface to fabricate the PD. The surface morphologies of both $\beta$-$Ga_2O_3$ and Si-doped GaN thin films were characterized by scanning electron microscopy (SEM) and atomic force microscopy (AFM). The crystalline structures of the samples were investigated using x-ray diffraction (XRD) analysis. Optical absorption measurements were performed through UV-visible (UV-vis) spectroscopy to determine the optical band gaps of the deposited films. In addition, the energy band alignment was precisely determined by ultraviolet photoelectron spectroscopy (UPS) measurements. To comprehensively evaluate the optoelectronic characteristics of the device, photoresponse measurements were performed under 254-nm and 365-nm ultraviolet illumination using a Keysight B1505A power device analyzer.

## 3. Results and discussion

The surface morphologies of the Si–GaN and $\beta$-$Ga_2O_3$ films are characterized by scanning electron microscopy (SEM) (Figs. 1(b) and 1(c)), which exhibit relatively uniform and smooth surfaces. The AFM images of Si–GaN and $Ga_2O_3$ are inserted in Figs. 1(b) and 1(c) respectively and show the surface morphology of the thin film with a scanning area of 2 μm×2 μm. The root-mean-square (RMS) surface roughness values are 0.44 nm and 2.79 nm, respectively. The surface of $Ga_2O_3$ thin film is rougher than that of the Si–GaN thin film, which may be caused by the large lattice mismatch between $Ga_2O_3$ and the underlying GaN during PECVD growth. A distinct interfacial boundary between the two materials is clearly observed in the cross-sectional SEM image (Fig. 1(d)). The measured thicknesses of the GaN film and PECVD-deposited $\beta$-$Ga_2O_3$ layer are determined to be 4.25 μm and 377 nm, respectively.

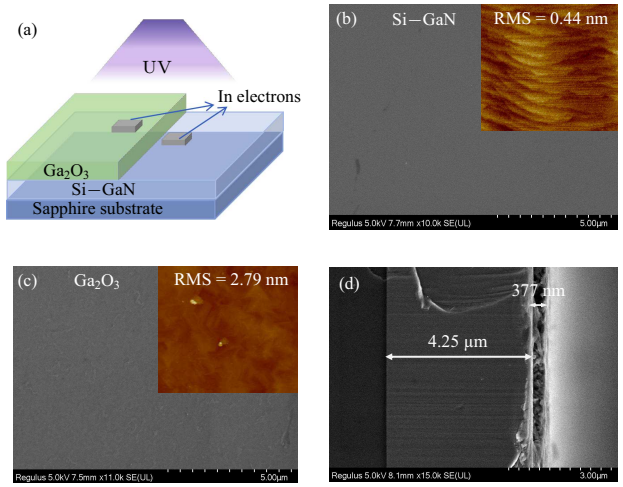



**Fig. 1.** (a) Schematic diagram of the Si–GaN/$\beta$-$Ga_2O_3$ heterojunction PD. The SEM (b) surface image of the Si–GaN (the inset is the AFM image) and (c) $\beta$-$Ga_2O_3$ film (the inset is the AFM image); (d) cross-section image of the Si–GaN/$\beta$-$Ga_2O_3$ heterojunction.

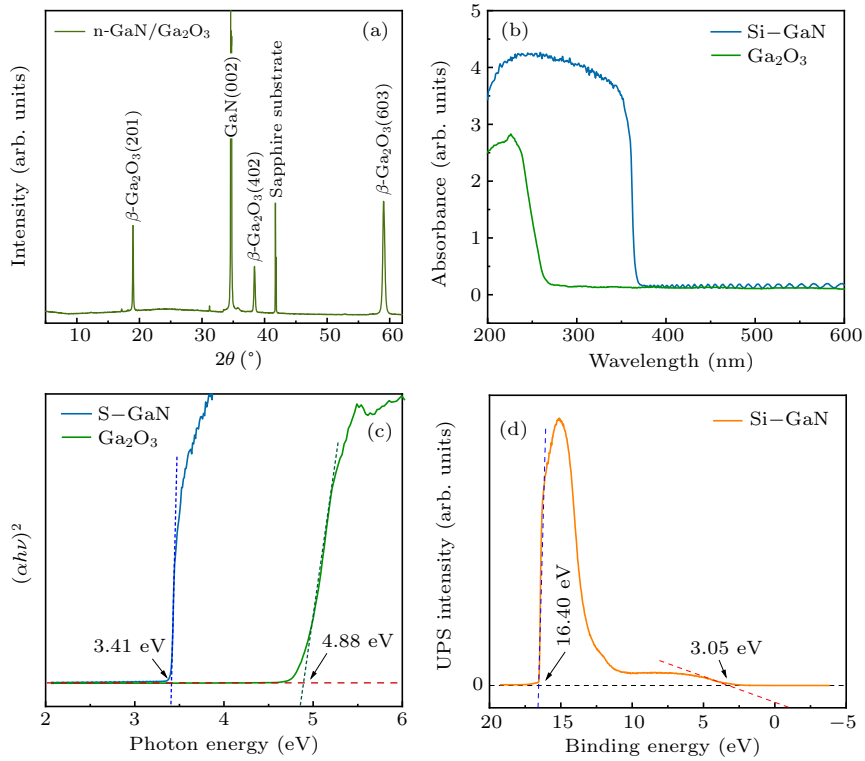



**Fig. 2.** (a) XRD patterns of the Si–GaN/$\beta$-$Ga_2O_3$ heterojunction. (b) Absorption spectra of $\beta$-$Ga_2O_3$ and GaN films. (c) Optical band gaps of $\beta$-$Ga_2O_3$ and GaN films. (d) The UPS spectrum of the Si–GaN film.

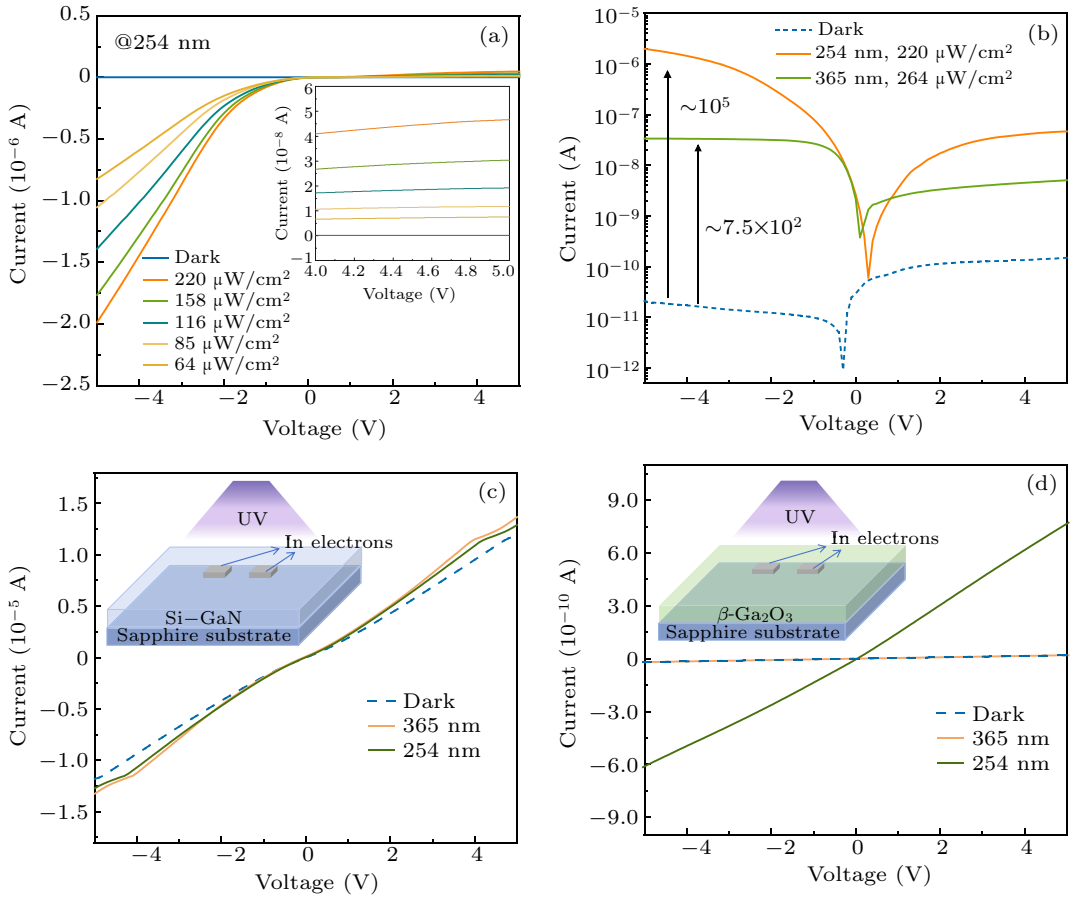



**Fig. 3.** (a) *I–V* characteristic curve of the Si–GaN/$\beta$Ga$_2$O$_3$ n–n junction photodetector under 254-nm light illumination, (b) the log-scale *I–V* curves of Si–GaN/$\beta$Ga$_2$O$_3$ PD under different wavelength light; *I–V* characteristic curve of (c) In/Si–GaN/In MSM structure in dark, under 365-nm light and 254-nm light illumination; (d) In/$\beta$Ga$_2$O$_3$/In MSM structure in dark, under 365-nm light and 254-nm light illumination.

The x-ray diffraction (XRD) analysis of the Si–GaN/$\beta$-Ga$_2$O$_3$ heterojunction is shown in Fig. 2(a). In addition to the prominent diffraction peaks originating from the sapphire substrate, three characteristic peaks located at 18.88°, 38.37°, and 58.92° are identified, which are indexed to $(\bar{2}01)$, $(\bar{4}02)$, and $(\bar{6}03)$ crystallographic planes of $\beta$-Ga$_2$O$_3$, respectively.[16] Furthermore, an additional diffraction peak is observed at 34.65°, corresponding to the (002) plane of wurtzite GaN.[6] The UV-vis absorbance spectrum of $\beta$-Ga$_2$O$_3$ and Si–GaN were illustrated in Fig. 2(b), from which the optical $E_g$ of the $\beta$-Ga$_2$O$_3$ and Si–GaN thin films can be evaluated according to the Tauc's relationship[16]

$$(\alpha h\nu)^2 = C(h\nu - E_g), \tag{1}$$

where $C$ is a constant and $h\nu$ is the photon energy of the incident light. By extrapolating the function of $(\alpha h\nu)^2$ and $h\nu$, $E_g$ of the $\beta$-Ga$_2$O$_3$ and Si–GaN thin films are determined to be 4.88 eV and 3.41 eV respectively (Fig. 2(c)). Moreover, UPS was conducted to identify the energy band diagram of Si–GaN, as shown in Fig. 2(d). The calculated work function of Si–GaN is $21.22 - 16.40 = 4.82$ eV, where 21.22 is the energy value of helium discharge lamp photons. Additionally, the valence band edge values (relative to the Fermi level) is extracted to be 3.05 eV.

The linear *I–V* characteristics of the heterojunction photodetector under dark and 254-nm light illumination with various light intensities are demonstrated in Fig. 3(a). Under 254-nm illumination, the PD exhibits rectification behavior, with an open-circuit voltage ($V_{oc}$) of approximately 400 mV, confirming the presence of a built-in electric field and its self-powered operation capability. The semilog *I–V* characteristics of the heterojunction photodetector under dark, 254-nm and 365-nm illumination are displayed in Fig. 3(b). Under a bias voltage of −5-V and 254-nm illumination, the photocurrent increases sharply, achieving a PDCR of $10^5$, which is two orders of magnitude higher than that obtained under 365-nm illumination.

Additionally, to exclude the influence of the contact between the thin film and the electrode on the device performance, we studied the contacts at the In/Si–GaN/In and In/$\beta$Ga$_2$O$_3$/In interfaces. The *I–V* curve of the In/Si–GaN/In MSM structure is shown in Fig. 3(c) and the schematic diagram of the MSM structure device is shown in the inset. The linear characteristic of the *I–V* curve indicates an Ohmic contact between the Si–GaN and In electrodes.[17] Under 254-nm and 365-nm light illumination, the photocurrent shows a slight increase compared to those under dark conditions. Meanwhile, the relatively low resistance of the GaN thin film leads to a high dark current in the GaN film. The *I–V* curve of

the In/$\beta$$Ga_2O_3$/In MSM structure is shown in Fig. 3(d). The results confirm that the In electrode forms an Ohmic contact with the $\beta$$Ga_2O_3$ thin film, and the photoresponse under 254-nm light illumination is more sensitive than that under 365-nm light illumination. These results validate confirming the device response is dominated by the n–n heterojunction itself.

As illustrated in Fig. 4(a), the $I$–$t$ characteristics of the photodetector under 254-nm illumination with different light intensities at zero bias are presented. The photogenerated electron–hole pairs are effectively separated by the built-in electric field, with electrons drifting from GaN to $Ga_2O_3$, resulting in a negative current. When the light intensity increases to 220 μW/cm$^2$, $I_{photo}$ gradually increases and reaches up to 3.5 nA.

Furthermore, as shown in Fig. 4(b), under identical illumination intensity, the current generated under 254-nm illumination is significantly higher than that under 365-nm illumination. This phenomenon can be attributed to the higher density of photogenerated carriers produced in the heterojunction under 254-nm illumination, leading to a more efficient separation of electron–hole pairs by the built-in electric field. Moreover, the built-in electric field induced under 254-nm illumination is stronger, which not only enhances the carrier separation efficiency but also provides a greater driving force for charge transport while suppressing electron–hole recombination, thereby generating a larger self-powered current.

At the same time, it can be seen from the figure that the self-powered current generated under zero bias voltage has an obvious overshoot phenomenon. When the ultraviolet lamp is turned on, the carrier concentration overshoots due to the rapid injection of photogenerated carriers, producing an obvious spike before the current reaches a stable state. However this process is very short, and the current will soon return to stability. When a bias voltage is applied, the photogenerated electrons and holes are propelled by the external electric field to drift in the antiparallel directions. This directional migration effectively eliminates the overshooting phenomenon, as shown in Fig. 4(c).

Under the 254-nm light illumination with a light intensity of 220 μW/cm$^2$, the transient response speed at zero bias voltage was estimated by fitting the equation[18]

$$I = I_0 + A\,\mathrm{e}^{-t/\tau_1} + B\,\mathrm{e}^{-t/\tau_2}. \tag{2}$$

As shown in Fig. 4(d), the device exhibits non-competitive rise times ($\tau_{r1}$ = 0.19 s and $\tau_{r2}$ = 1.41 s) and decay times ($\tau_{d1}$ = 0.25 s and $\tau_{d2}$ = 2.94 s). The relatively long response time can be primarily attributed to lattice mismatch during the heterojunction epitaxy. This structural mismatch introduces interfacial trap states that temporarily capture the carriers. When these trapped carriers are subsequently released or recombined, they introduce additional delays in carrier separation. Furthermore, the energy band discontinuities at the heterojunction interface form potential barriers, thereby causing electron accumulation at the interface and prolonging the rise time.

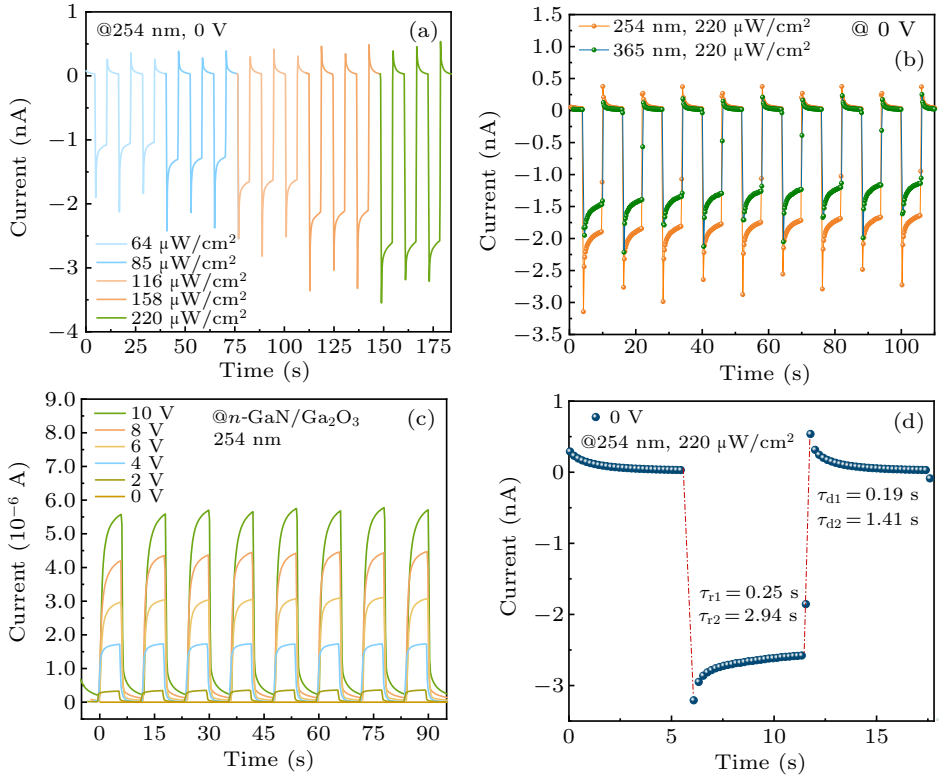



**Fig. 4.** Continuous time-dependent photoresponse of the Si–GaN/$Ga_2O_3$ n–n junction photodetector under zero bias at (a) various 254-nm light intensities; (b) 254-nm and 365-nm, 220-μW/cm$^2$ illumination; (c) various bias voltages under 254-nm light illumination with an intensity of 220 μW/cm$^2$; (d) fitting response times under 254-nm light illumination with an intensity of 220 μW/cm$^2$ at 0 V.

Figure 5(a) shows the band structure diagram of Si–GaN and $\beta$-$Ga_2O_3$ before contact. Due to the difference in electron affinity between the two materials, an offset exists in their conduction band minimum positions. When an interface is formed between them (Fig. 5(b)), a sudden energy level shift occurs at the conduction band edge. This conduction band step hinders electron transport from $\beta$-$Ga_2O_3$ to Si–GaN.[19,20] In the absence of an external electric field, electrons spontaneously migrate from the material with a higher Fermi level to the material with a lower Fermi level until the Fermi levels of both materials reach equilibrium.[21] During this process, electrons are transferred from the $\beta$-$Ga_2O_3$ side to the Si–GaN side, resulting in the formation of an electron depletion layer at the $\beta$-$Ga_2O_3$ interface and an electron accumulation layer at the Si–GaN interface. This charge redistribution creates a built-in electric field directed from $\beta$-$Ga_2O_3$ to Si–GaN, accompanied by upward band bending in Si–GaN and downward band bending in $\beta$-$Ga_2O_3$. Under illumination, photogenerated carriers (electron–hole pairs) are effectively separated by the built-in electric field and electrons are driven toward the $\beta$-$Ga_2O_3$ side, generating a self-powered current flowing from $\beta$-$Ga_2O_3$ to Si–GaN. As shown in Fig. 5(c), when a forward bias (Si–GaN connected to the positive electrode) is applied, the external electric field opposes the built-in electric field, thereby reducing the overall field strength. In this case, the separation efficiency of the photogenerated carriers is reduced, and the conduction band step further impedes electron backflow to Si–GaN, resulting in a relatively small photocurrent. Conversely, under reverse bias (Fig. 5(d)), the external electric field aligns with the built-in electric field, enhancing the overall field effect. The carrier separation efficiency is improved and the carrier recombination process is suppressed, thereby yielding a larger photocurrent. This asymmetric current characteristic demonstrates a typical rectification.

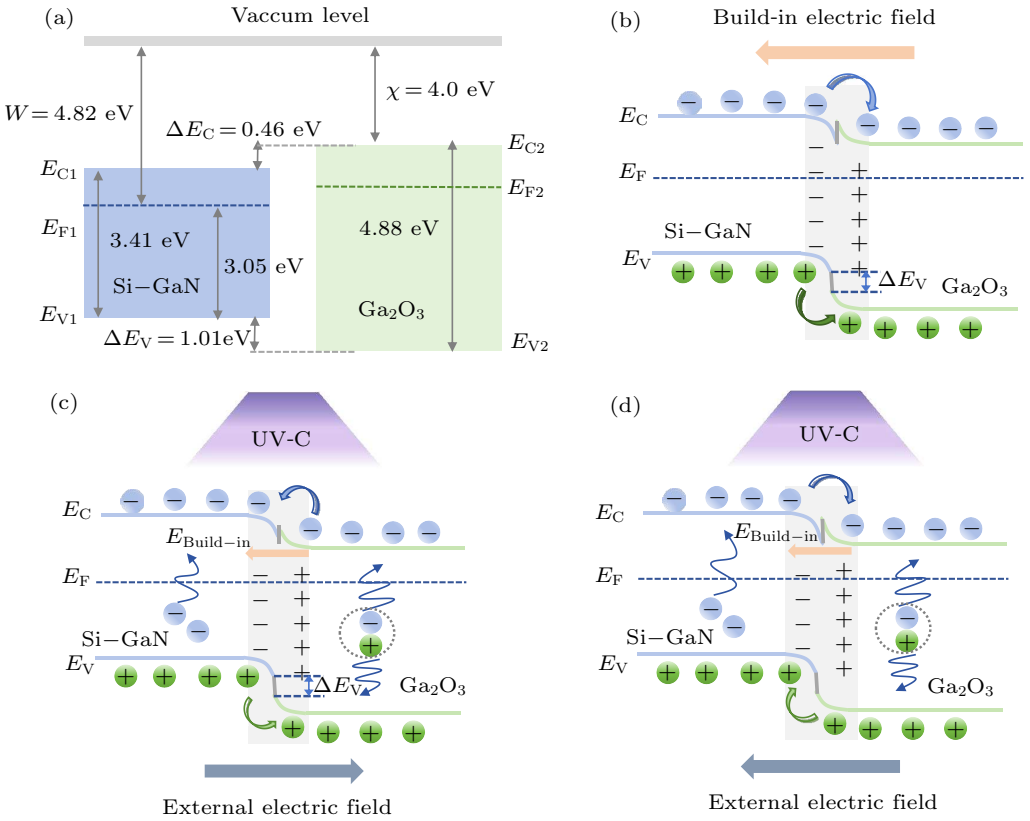



**Fig. 5.** Energy band alignment of Si–GaN and $\beta$-$Ga_2O_3$ (a) before contact; (b) after contact; the operating mechanism and equivalent circuit model of the heterojunction-based photodetector at (c) positive voltage and (d) negative voltage under UV illumination.

To comprehensively explore the performance of the Si–GaN/$\beta$-$Ga_2O_3$ photodetector, we determined the $R$, $D^*$, and external quantum efficiency (EQE) at zero bias as they vary with different light intensities. The $R$, EQE, $D^*$, and PDCR were derived as follows:[22,23]

$$R = \frac{I_{\text{photo}} - I_{\text{dark}}}{P \cdot S}, \tag{3}$$

$$D^* = \frac{R\sqrt{S}}{\sqrt{2eI_{\text{dark}}}}, \tag{4}$$

$$\text{EQE} = \frac{hcR}{e\lambda}, \tag{5}$$

$$\text{PDCR} = \frac{I_{\text{photo}} - I_{\text{dark}}}{I_{\text{dark}}}, \tag{6}$$

where $P$ is the light intensity, $S$ is the effective illuminated area of the PD, $e$ is the electron charge, $h$ is Planck's constant, $\lambda$ is the wavelength, and $c$ is the speed of light. As shown in Fig. 6(a), with increasing incident light intensity, more electron–hole pairs are generated and a self-heating ef-

fect is introduced. The probability of charge carrier scattering and recombination increases, resulting in a decrease in $R$. According to the formula, it can be seen that both EQE and $D^*$ will decrease as $R$ decreases. Under the 254-illumination with a light intensity of 64 μW/cm$^2$, $R$, EQE, and $D^*$ are calculated to be 0.475 mA/W, 0.24%, and $8.6\times10^8$ Jones at 0 V, respectively. As illustrated in Fig. 6(b), the photocurrent grows with increasing light intensity, which can be fitted to the power law $I \propto P^{\theta}$,[15] with $\theta = 0.52$. The parameter $\theta$ serves as an exponent characterizing. The photoresponse magnitude. This phenomenon implies the existence of abundant intrinsic defects within the heterojunction. These defects are presumably induced by oxygen plasma bombardment during PECVD growth of $\beta$-$Ga_2O_3$ on Si–GaN, which degrades the Si–GaN surface and introduces defects, and interfacial states generated by lattice mismatch at the heterojunction interface. The trap states capture the photogenerated carriers, leading to nonlinear recombination processes. This effect is notably pronounced under low light intensities, exhibiting sublinear photoresponse behavior ($\theta < 1$).[13] Additionally, figure 6(c) shows the PDCR values under different light intensities as they change with the applied bias voltages. The PDCR, which characterizes the detector's signal-to-noise ratio, exhibits a substantial increase as the light intensity rises. When a −5-V bias is applied and the device is illuminated with 254-nm light at an intensity of 220 μW/cm$^2$, the PDCR reaches a remarkable $\sim 10^5$, highlighting the n–n type heterojunction photodetector's exceptional photoresponse.

The comparison between the performances of the Si–GaN/$\beta$-$Ga_2O_3$ heterojunction photodetector in this work and $Ga_2O_3$-based heterojunction photodetectors in other reports is listed in Table 1, demonstrating that our heterojunction exhibits lower dark current, relatively good responsivity at an applied voltage of 0 V, and demonstrates certain potential for applications in the field of self-powered photodetectors.

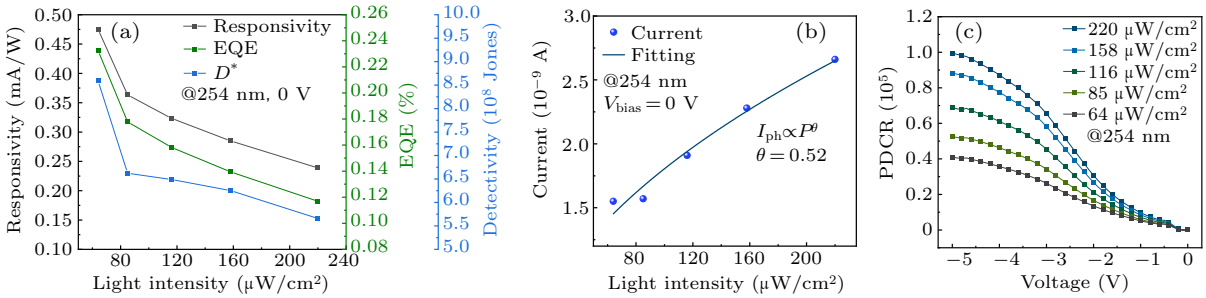



**Fig. 6.** (a) Responsivity, external quantum efficiency, and detectivity as a function of the light intensities at 0 bias under 254-nm light illumination. (b) The fitted nonlinear relation curve of the photocurrent with the light intensities; (c) photo-to-dark current ratios as a function of applied bias voltages under various 254-nm light intensities of the heterojunction photodetector.

**Table 1.** Comparisons of the performances of $Ga_2O_3$-based heterojunction photodetectors.

| Photodetector | $I_{dark}$ (A) | PDCR | $R$ (mA/W) | $D^*$ (Jones) | Ref. |
|---|---|---|---|---|---|
| Si–GaN/$\beta$-$Ga_2O_3$ | $2.96\times10^{-11}$ (0 V) | $1\times10^5$ (220 μW/cm$^2$) | 0.475 (0 V) | $8.6\times10^8$ (0 V) | this work |
| $La_2O_3$/$\varepsilon$-$Ga_2O_3$ | – | $2.68\times10^4$ (220 μW/cm$^2$) | 1.67 (0 V) | – | [24] |
| $\beta$-$Ga_2O_3$ nanoflakes/p-Si | $2.33\times10^{-9}$ (0 V) | $4.8\times10^4$ (7000 W/cm$^2$) | 0.16 (0 V) | – | [25] |
| $\beta$-$Ga_2O_3$/NiO | $3.35\times10^{-11}$ (0 V) | – | 0.245 (0 V) | $1.81\times10^8$ (0 V) | [26] |
| PEDOT: PSS/$Ga_2O_3$ | $9.5\times10^{-7}$ (0 V) | – | 0.24 (0 V) | – | [27] |
| $Ga_2O_3$/$CuGaO_2$ | $5.1\times10^{-14}$ (0 V) | $2.3\times10^4$ (1000 μW/cm$^2$) | 0.025 (0 V) | $9\times10^{10}$ (0 V) | [28] |
| $Ga_2O_3$/$CuCrO_2$ | $6.1\times10^{-14}$ (0 V) | $3.5\times10^4$ (1000 μW/cm$^2$) | 0.12 (0 V) | $4.6\times10^{11}$ (0 V) | [28] |

## 4. Conclusion

An n–n heterojunction photodetector based on Si–GaN/$\beta$-$Ga_2O_3$ is successfully fabricated via PECVD. The device exhibits outstanding detection performance under 254-nm ultraviolet illumination: at zero bias with 64-μW/cm$^2$ intensity, it achieves an $R$ of 0.475 mA/W and a specific $D^*$ of $8.6\times10^8$ Jones. A significant self-powered photocurrent of 3.5 nA is observed at 220 μW/cm$^2$, demonstrating a linear response to increasing light intensity. Under −5-V reverse bias, the device shows exceptional photoresponse characteristics, including an ultrahigh photo-to-dark current ratio (PDCR) of $\sim 10^5$. This study demonstrates a cost-effective fabrication strategy for n–n heterojunction photodetectors. The device delivers p–n junction-comparable performance in self-powered UV detection, highlighting the substantial potential of n–n junction architectures for optoelectronic applications.

## Acknowledgements

Project supported by the Joints Fund of the National Natural Science Foundation of China (Grant No. U23A20349) and the Young Scientists Fund of the National Natural Science Foundation of China (Grant Nos. 62204126, 62305171, and 62304113).

## References


[1] Kaur D and Kumar M 2021 *Adv. Opt. Mater.* **9** 2002160

[2] Xu J J, Zheng W and Huang F 2019 *J. Mater. Chem. C.* **7** 8753

[3] Xie C, Lu X T, Tong X W, Zhang Z X, Liang F X, Liang L, Luo L B and Wu Y C 2019 *Adv. Funct. Mater.* **29** 1806006

[4] Qin Y, Long S, Dong H, He Q, Jian G, Zhang Y, Hou X, Tan P, Zhang Z, Lv H, Liu Q and Liu M 2019 *Chin. Phys. B.* **28** 018501

[5] Zhang J, Kuang X, Tu R and Zhang S 2024 *Adv Colloid Interface Sci.* **328** 103175

[6] Chu R 2020 *Appl. Phys. Lett.* **116** 090502

[7] Yue J Y, Ji X Q, Li S, Qi X H, Li P G,Wu Z P and Tang W H 2023 *Chin. Phys. B* **32** 016701

[8] Guo D Y, Su Y L, Shi H Z, Li P G, Zhao N, Ye J H, Wang S L, Liu A P, Chen Z W, Li C R and Tang W H 2018 *ACS Nano* **12** 12827

[9] Jiang J L, Luo J S, Ding K, Tang Y, Zhang H, Ye L J, Pang D, Li H and Li W J 2025 *Small* **21** e2406447

[10] Singh A, Koksal O, Tanen N, McCandless J, Jena D, Xing H and Peelaers H 2020 *Appl. Phys. Lett.* **117** 072103

[11] X S Fang, Z Q Li and Y Hu 2023 *J. Inorg. Mater.* **38** 1055

[12] M X Cheng, S Z Luan, H L Wang and R X Jia 2023 *Chin. Phys. B* **32** 037302

[13] Yang L L, Peng Y S, Liu Z, Zhang M L, Guo Y F, Yang Y and Tang W H 2023 *Chin. Phys. B* **32** 047301

[14] Wu C, Guo D Y, Zhang L Y, Li P G, Zhang F B, Tan C K, Wang S L, Liu A P, Wu F M and Tang W H 2020 *Appl. Phys. Lett.* **116** 072102

[15] Yang L L, Liu Z, Li S, Zhang M L, Xi Z Y, Xu Q, Yan S H, Guo Y F and Tang W H 2024 *IEEE Electron Dev. Lett.* **45** 420

[16] Tauc J, Grigorovici R and Vancu A 1966 *Phys. Status Solid B* **15** 627

[17] Li P G, Shi H Z, Chen K, Guo D Y, Cui W, Zhi Y S, Wang S L, Wu Z P, Chen Z W and Tang W H 2017 *J. Mater. Chem. C* **5** 10562

[18] Liu N, Fang G, Zeng W, Zhou H, Cheng F, Zheng Q, Yuan L, Zou X and Zhao X 2010 *ACS Appl. Mater. Interface* **2** 1973

[19] Wang K, Lian C, Su N, Jena D and Timler J 2007 *Appl. Phys. Lett.* **91** 232117

[20] Zeng H, Wang W, Ivanov I G, Darakchieva V and Sun J 2024 *Appl. Phys. Lett.* **125** 162102

[21] Li S, Zhi Y S, Lu C, Wu C, Yan Z Y, Liu Z, Yang J, Chu X L, Guo D Y, Li P G, Wu Z P and Tang W H 2021 *J. Phys. Chem. Lett.* **12** 447

[22] Kong W Y, Wu G A, Wang K Y, Zhang T F, Zou Y F, Wang D D and Luo L B 2016 *Adv. Mater.* **28** 10725

[23] Guo X C, Hao N H, Guo D Y, Wu Z P, An Y H, Chu X L, Li L H, Li P G, Lei M and Tang W H 2016 *J. Alloys Compd.* **660** 136

[24] Xi Z Y, Liu Z, Yang L L, Tang K, Li L, Shen G H, Zhang M L, Li S, Guo Y F and Tang W H 2023 *Appl. Mater. Interfaces* **15** 40744

[25] Atilgan A, Yildiz A, Harmanci U, Gulluoglu M T and Salim K 2020 *Mater. Today Commun.* **24** 101105

[26] Yu J G, Yu M, Wang Z, Yuan L, Huang Y, Zhang L C, Zhang Y M and Jia R X 2020 *IEEE Trans. Electron Dev.* **67** 3199

[27] Wu C, He H L, Hu H Z, Liu A P, Wang S L, Guo D Y and Wu F M 2023 *Journal of Semiconductors* **44** 58

[28] Wu C 2020 *Mater. Today Phys.* **17** 100335